MINFLUX reveals dynein stepping in live neurons

Jonas M. Schleske[a], Jasmine Hubrich[a], Jan Otto Wirth[a], Elisa D'Este[a], Johann Engelhardt[a], and Stefan W. Hell[a,b,1] 📷

Affiliations are included on p. 7.

Dynein is the primary molecular motor responsible for retrograde intracellular transport of a variety of cargoes, performing successive nanometer-sized steps within milliseconds. Due to the limited spatiotemporal precision of established methods for molecular tracking, current knowledge of dynein stepping is essentially limited to slowed-down measurements in vitro. Here, we use MINFLUX fluorophore localization to directly track CRISPR/Cas9-tagged endogenous dynein with nanometer/millisecond precision in living primary neurons. We show that endogenous dynein primarily takes 8 nm steps, including frequent sideways steps but few backward steps. Strikingly, the majority of direction reversals between retrograde and anterograde movement occurred on the time scale of single steps (16 ms), suggesting a rapid regulatory reversal mechanism. Tug-of-war-like behavior during pauses or reversals was unexpectedly rare. By analyzing the dwell time between steps, we concluded that a single rate-limiting process underlies the dynein stepping mechanism, likely arising from just one adenosine 5′-triphosphate hydrolysis event being required during each step. Our study underscores the power of MINFLUX localization to elucidate the spatiotemporal changes underlying protein function in living cells.

MINFLUX | fluorescence nanoscopy | dynein | CRISPR/Cas9 | live neurons

Axons are the longest processes of neurons, reaching lengths of millimeters to meters. For rapid and targeted movement of cellular components such as mitochondria, organelles, proteins, or RNA between the soma and the axon terminal, a directed, nondiffusive transport mechanism is essential (1, 2). Due to the crucial role of intracellular transport in neuronal development and cellular integrity, several neurological diseases are associated with axonal transport impairment (3, 4). Axonal transport is facilitated by the kinesin motor protein family and cytoplasmic dynein 1 (hereafter dynein), which move in opposite directions on the unidirectionally oriented microtubules in the axon (5–7). For retrograde transport, one or two dynein dimers are assembled with dynactin and a specific activating adaptor tethered to the cargo (8–11).

Dynein has been studied extensively over the past two decades. The use of artificially dimerized, truncated yeast dynein monomers in vitro revealed that dynein moves toward the minus end of microtubules in steps of high variability (12, 13), relying on a proposed flexible and uncoordinated stepping mechanism (13–15). Furthermore, highly variable step sizes between 8 and 32 nm, including frequent sideways and backward steps, were observed using purified human and mammalian dynein motor complexes (16, 17). Additionally, it was found that the dynein motor complexes take smaller steps, mainly 8 nm in size, under load (16, 17). However, due to the limited spatiotemporal precision, either individual steps could not be resolved in live cells (18, 19), or drastically reduced adenosine 5′-triphosphate (ATP) concentrations were used to slow down the dynein motor (complex) movement and allow single-step observation in vitro (12–17). As a result, the current understanding of the dynein stepping behavior is largely based on decidedly slowed-down in vitro movements, raising the question of how endogenous dynein actually steps in a living cell. Although cargo and large artificial cargo serving as optical probes (scattering or fluorescent beads >50 nm in diameter) have been tracked with high precision in living cells (20–22), it is challenging to extrapolate these observations to the dynein stepping itself. Direct tracking of endogenous dynein in living cells requires a method to resolve the dynein steps with a specific minimally invasive label that is substantially smaller than the protein itself.

Recently, MINFLUX has been demonstrated to be capable of directly tracking protein dynamics and conformational changes, such as those of kinesin-1 (23, 24), by the use of a minimally invasive fluorescent label. MINFLUX localizes a fluorophore by relating its unknown position to the known position of the central intensity minimum (zero) of a

fluorescence excitation beam (25). Reducing the distance between the two positions, i.e., matching them as closely as possible, increases the localization precision per detected fluorescence photon. Practical MINFLUX typically requires only about 100 detected photons to achieve single-digit nanometer localization precision, meaning that a spatiotemporal precision of a few nanometers per millisecond is readily achieved. In contrast, popular fluorophore localization methods that rely on the identification of the maximum of the fluorescence diffraction pattern produced by the fluorophore on a camera (i.e., centroid calculation) require about one hundred times more detected photons per fluorophore (26). Consequently, to achieve comparable spatiotemporal precision, established methods require photon-detection rates that are accordingly higher. In many cases, these rates can be provided only by strongly scattering labels, such as beads, that are many times larger than the protein to be observed.

Here, we use MINFLUX localization and a label that is considerably smaller than the protein under observation to directly track endogenous mammalian dynein with nanometer/millisecond precision in a primary culture of living hippocampal neurons. Using a CRISPR/Cas9-mediated knock-in approach, we were able to specifically and directly tag dynein at two different sites and label them with a fluorophore. Our observations revealed that endogenous tail-labeled dynein performs mainly 8 nm steps along the microtubule, as well as frequent sideways but few backward steps. Most notably, direction reversals between retrograde and anterograde movement occurred on the time scale of individual steps, suggesting a rapid regulatory reversal mechanism. The analysis of the dwell time between steps led us to conclude that a single rate-limiting process underlies the dynein stepping mechanism, indicating that dynein requires a single ATP molecule per step.

Direct and Site-Specific CRISPR/Cas9-Mediated Endogenous Tagging of Mammalian Dynein in Live Primary Neurons.
Overexpression of individual dynein subunits has been shown to affect the integrity of the entire motor complex and endomembrane localization (27, 28). To avoid overexpression, we used CRISPR/Cas9-mediated endogenous tagging to directly and specifically tag dynein for subsequent study of its stepping behavior (29). For each dynein-specific target sequence (*SI Appendix*, Table S1), we designed and generated an ORANGE-based (30) plasmid for the knock-in of a HaloTag (31) at either the N terminus of the dynein heavy chain (Halo-DHC) or the N terminus of the dynein intermediate chain (Halo-DIC) (*SI Appendix*, Fig. S1 and Table S2). Correct and specific integration of the HaloTag sequence at the dynein loci was assessed by sequencing the isolated genomic DNA of primary rat hippocampal neurons electroporated with each plasmid.

To visualize endogenous dynein in living neurons, we electroporated primary rat hippocampal neurons with one of our CRISPR/Cas9 knock-in plasmids. After six to nine days in culture, we labeled Halo-DHC and Halo-DIC with MaP555-Halo (32) and performed widefield microscopy tracking of endogenous dynein on stained microtubules (Fig. 1*A*). Thus, the Halo-DHC and Halo-DIC positive neurons were readily distinguishable from the wildtype neurons, and the axon was clearly identifiable as the longest and smoothest process (Fig. 1 *B* and *D*). We followed the axon for several hundred microns, recorded videos of labeled dynein, and generated kymographs of Halo-DHC (Fig. 1*C*) and Halo-DIC (Fig. 1*E*). To distinguish between retrograde and anterograde movements, we applied Fourier filtering to the kymographs (33, 34). In accordance with a recent study of endogenously tagged dynein in induced neurons (35), the majority of dynein was not processive.

Instead, only a small fraction showed retrograde movement, including direction reversals and pauses (Fig. 1 *C* and *E* and *SI Appendix*, Fig. S2 and Movie S1), as previously observed for various intracellular cargoes (21, 36–40) and GFP-tagged DIC (41). Both processive Halo-DHC and Halo-DIC tagged motor complexes moved similarly fast in the retrograde direction [DHC: (1.1 ± 0.4) µm s^{-1}, DIC: (1.5 ± 0.7) µm s^{-1}, median ± median absolute deviation, MAD] with speeds up to 4 µm s^{-1}, comparable to speeds reported for endogenously tagged dynein in induced neurons (35), prion protein (38), or amyloid precursor protein vesicles (42). Limitations to widefield tracking of individual dynein motors were set by nonprocessive labeled dynein molecules but also by photobleaching and out-of-focus movement. In any case, CRISPR/Cas9-mediated endogenous tagging turned out to be highly suitable for direct and site-specific labeling of dynein in living primary neurons.

MINFLUX Reveals Stepping Behavior of Endogenous Dynein.
Next, we sought to investigate the stepping behavior of endogenous dynein. Again, we used our CRISPR/Cas9 knock-in plasmids to insert a HaloTag sequence into the dynein loci. To achieve single-molecule conditions and avoid having multiple labels per dynein motor complex, Halo-DHC or Halo-DIC were labeled with a low concentration of 100 pM JFX650-Halo (43). In a second step, the remaining dynein was saturated with MaP555-Halo (32) to identify Halo-Dynein positive neurons. Simultaneously, the microtubules of all neurons were labeled with BioTracker 488 to verify that MaP555-Halo was bound specifically to dynein on microtubules of only Halo-Dynein positive neurons (Fig. 2*A*).

To resolve individual steps of endogenous dynein, we used a MINFLUX microscope (44), whose nanometer/millisecond spatiotemporal precision is achieved by probing the current position of a single moving fluorophore with the intensity minimum of a donut-shaped 640 nm excitation beam (Fig. 2*B*). To ensure that only one emitter is localized at a time, the ratio of central to peripheral emission was calculated during tracking as a termination condition of the localization scheme (44). Using the MaP555-labeled dynein, we identified a Halo-DHC positive neuron and followed its axon over several hundred microns (Fig. 2*C*). Note that tubulin staining reveals a neighboring wild-type neuron, yet without colocalizing MaP555 emission, confirming the specificity of the labeling (Fig. 2*D*). Using this procedure, we were able to record MINFLUX traces of Halo-DHC in living neurons up to 1.6 µm in length and 3 s in duration in the retrograde and anterograde directions (*SI Appendix*, Fig. S3). We obtained a median localization precision of (3.5 ± 0.4) nm using a pattern diameter of L = 75 nm (*SI Appendix*, Table S4), which is comparable to state-of-the-art MINFLUX tracking studies (23, 24). For the recorded MINFLUX traces of Halo-DHC along the axon (Fig. 2 *E* and *F*), steps were identified using a bias-free step detection algorithm with no prior assumptions about step number or size (45); the algorithm only assumes that the traces contain steps. The resulting median step size uncertainty was (2.1 ± 0.6) nm.

To quantitatively characterize the stepping behavior of endogenous dynein, we classified all MINFLUX traces into retrograde and anterograde segments. The speed of Halo-DHC in both directions was similar (Fig. 2*G*) and comparable to the widefield recordings (Fig. 1*F*). Examining the detected steps in retrograde segments, most on-axis steps are approximately 8 nm in size, but the N terminus of the DHC (dynein tail) also takes larger steps up to 16 nm (Fig. 2*H*). Consistent with previous reports (12, 16), dynein frequently steps sideways (Fig. 2*I*), perhaps to circumvent obstacles
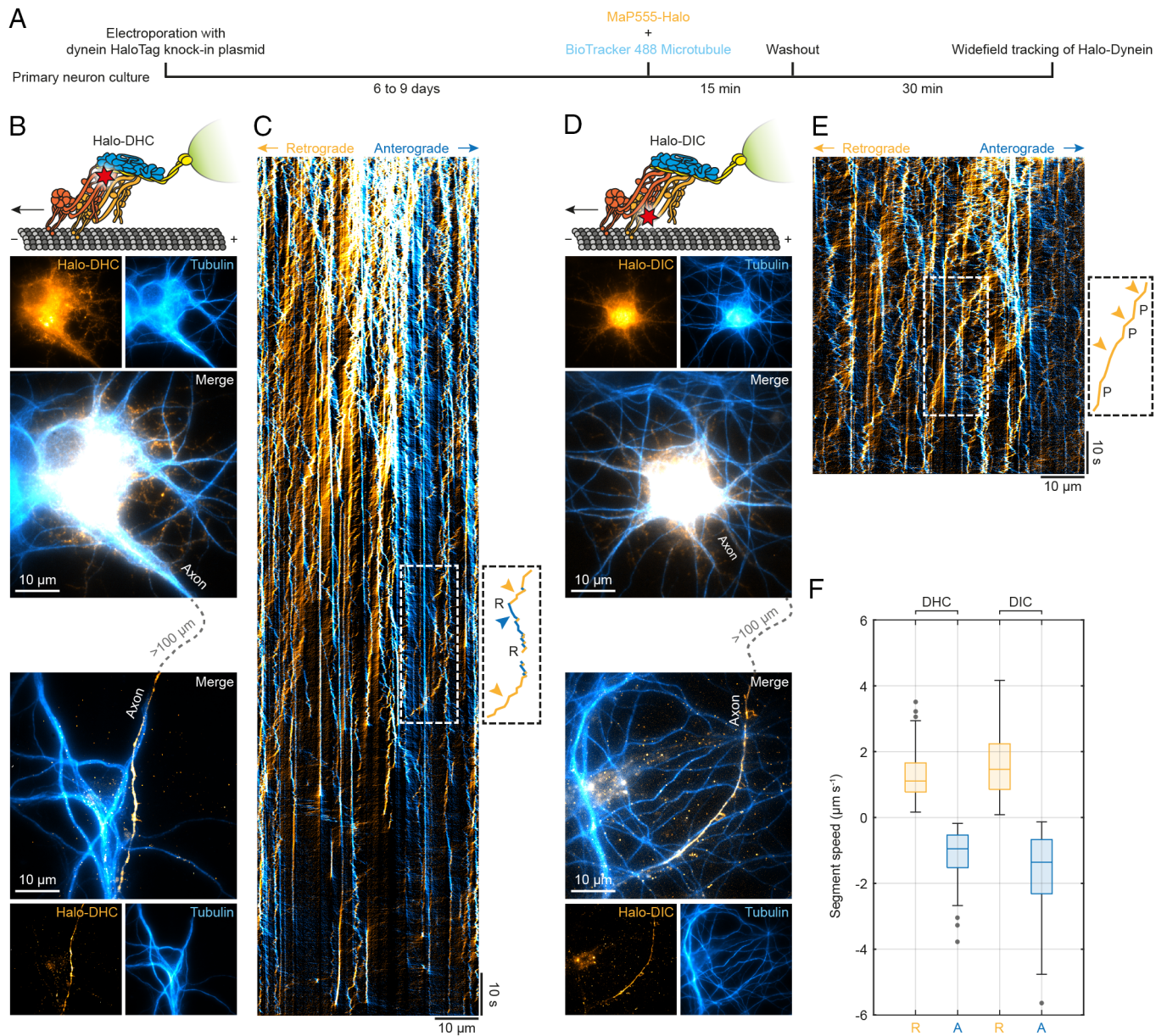
Fig. 1. Direct and specific CRISPR/Cas9-mediated endogenous tagging of dynein in live primary neurons. (*A*) Schematic of sample preparation for widefield tracking of endogenous dynein (Halo-DHC or Halo-DIC). Primary rat hippocampal neurons were electroporated with a CRISPR/Cas9 knock-in plasmid, resulting in N-terminal tagging of endogenous dynein with a HaloTag. After six to nine days in culture, dynein and microtubules were labeled simultaneously with cell-permeable dyes (MaP555-Halo and BioTracker 488 Microtubule), washed, and imaged. (*B*) Sketch of the Halo-DHC motor complex labeled with MaP555-Halo (red star), including dynactin (blue), an activating adaptor (yellow), and a cargo (green). Example widefield images (maximum intensity projection of video) showing the soma and axon of a Halo-DHC positive neuron and its microtubules, as well as those of neighboring neurons. Videos of labeled dynein were recorded along the axon, which was identified as the longest and smoothest process and traced for several hundred microns. (*C*) Example kymograph of Halo-DHC along the axon with retrograde movement colored in orange and anterograde movement colored in blue. Overlapping motion appears in white. The inset shows initial retrograde movement, which is followed by an instantaneous direction reversal (R) to anterograde movement, and a prolonged reversal to retrograde movement, as indicated by colored arrowheads. (*D*) Sketch of the Halo-DIC motor complex and example widefield images showing the soma and axon of a Halo-DIC positive neuron. Videos were acquired similarly to Halo-DHC. (*E*) Example kymograph of Halo-DIC along the axon, where the inset shows a retrograde movement interrupted by pauses (P). (*F*) Boxplot of segment speed of retrograde and anterograde motion from Halo-DHC (n = 329, 25 videos, N = 6) and Halo-DIC (n = 349, 22 videos, N = 4).

on the track (46), or also as an inherent consequence of dynein's long stalk domain and flexibility, which permits high variability in both on-axis and sideways steps. Occasionally, we also observed large sideways steps (>25 nm), suggesting a change to an adjacent microtubule or a step over several protofilaments at once (Fig. 2*F*). The distribution of dwell times between successive steps of Halo-DHC shows that the steps follow each other very quickly (half of the steps are faster than 7.4 ms), with the upper limit being approximately 100 ms (Fig. 2*J*).

A comparison of the stepping behavior of Halo-DIC to that of Halo-DHC reveals that the on-axis step size distribution of Halo-DIC (*SI Appendix*, Fig. S4*B*) is broader than that of Halo-DHC (Fig. 2*H*), exhibiting slightly larger steps and more frequent backsteps. Similarly, the off-axis distribution of Halo-DIC (*SI Appendix*, Fig. S4*C*) is also wider than that of Halo-DHC (Fig. 2*I*). These observations indicate that the DIC N terminus exhibits greater flexibility than the dynein tail while moving. This observation is consistent with structural studies indicating that the DIC N terminus is quite flexible (8, 47).
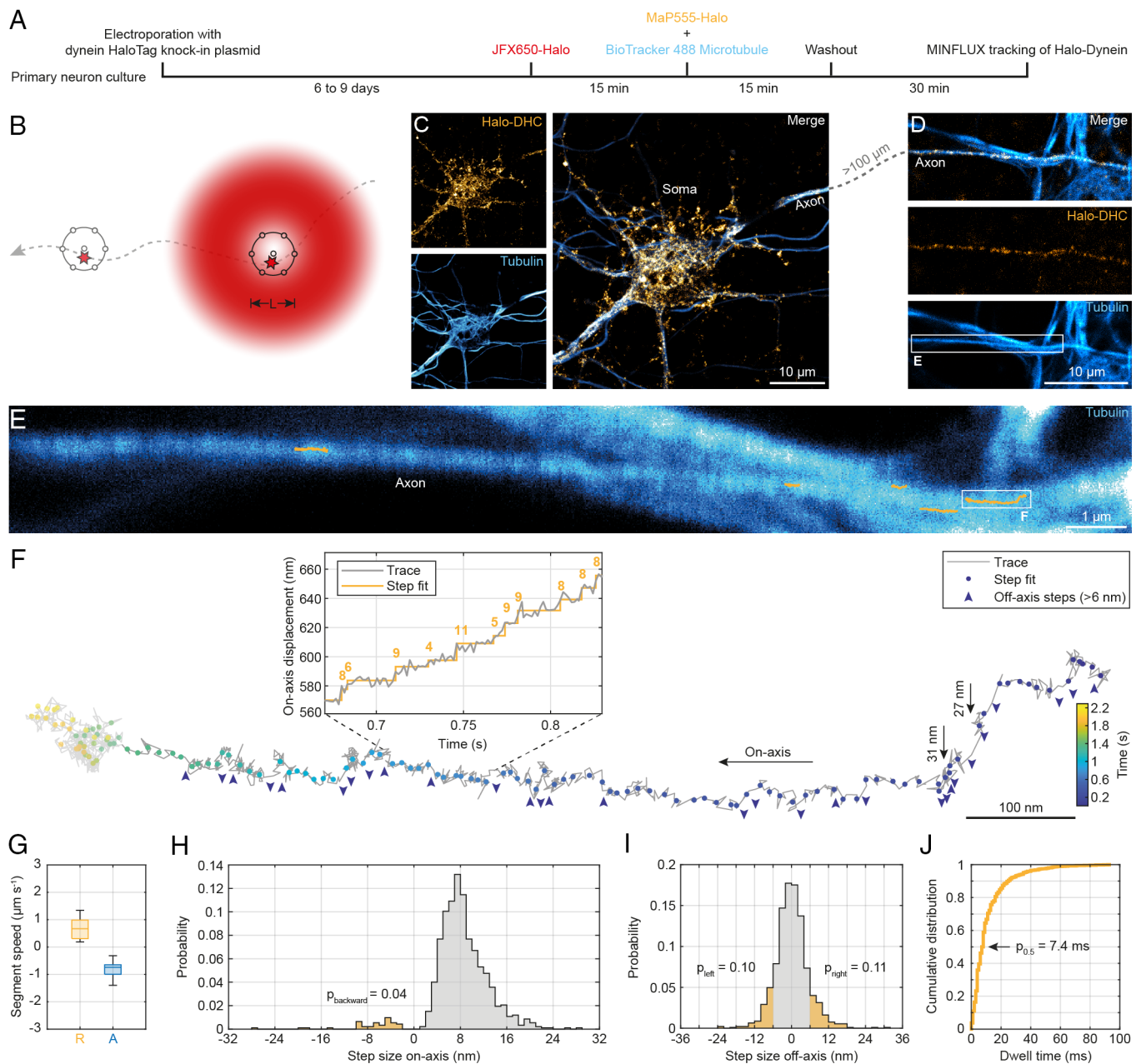
Fig. 2. MINFLUX reveals stepping behavior of endogenous dynein in live neurons. (*A*) Schematic of sample preparation for MINFLUX tracking of endogenous dynein. Primary rat hippocampal neurons were electroporated with a CRISPR/Cas9 knock-in plasmid, resulting in N-terminal tagging of endogenous dynein with a HaloTag. After six to nine days in culture, a fraction of dynein was labeled with 100 pM JFX650-Halo. The remaining dynein was labeled with 100 nM MaP555-Halo, and microtubules were simultaneously labeled. (*B*) MINFLUX procedure for tracking a single moving fluorophore (star on dashed trajectory). To determine the current position of the fluorophore with nanometer precision, a donut-shaped 640 nm excitation beam (red) probes seven positions (black circles) around the fluorophore with diameter L. This procedure is repeated during the fluorophore movement. (*C*) Example confocal images showing a Halo-DHC positive neuron and microtubules. (*D*) Confocal images showing the axon of the Halo-DHC positive neuron whose axon was traced over several hundred microns. The selected MINFLUX region of interest is highlighted by the white box. (*E*) Overlay of confocal image of tubulin with five MINFLUX traces of Halo-DHC (orange) along the axon. (*F*) Example of a MINFLUX trace of Halo-DHC with two large off-axis steps (black arrows) indicating a change of multiple protofilaments or a sideways step to an adjacent microtubule. Dots colored by time show the steps of dynein. Off-axis steps larger than 6 nm are indicated by blue arrowheads. The step sizes are shown in the on-axis displacement versus time plot. The left end of this trace (grayed out) was not included in further analysis because there was no processive movement in this region. (*G*) Boxplot of segment speeds in the retrograde (n = 25) and anterograde directions (n = 17) of Halo-DHC. (*H*) On-axis step size distribution of Halo-DHC with indicated proportion of backward steps (n = 925, N = 6). (*I*) Off-axis step size distribution of Halo-DHC with highlighted proportions of off-axis steps larger than 6 nm in either direction (n = 925, N = 6). (*J*) Cumulative distribution of dwell times between consecutive steps of Halo-DHC (n = 900, N = 6).

Overall, the on-axis step size distribution of the dynein tail (Fig. 2*H*) is narrower with smaller steps (4 to 16 nm) than in purified dynein motor complexes without load (8 to 32 nm) (16, 17). However, the distribution shows similarities to the in vitro distribution of dynein under high load (16, 48), which seems reasonable since dynein is only active in living cells when bound to a cargo. The mean forward step size of (8.7 ± 3.8) nm (*SI Appendix*, Table S5) is comparable to that observed for dynein

under high load in vitro (~10 nm) (16). This finding may suggest that dynein exerts a high force under endogenous conditions, assuming a molecular gear mechanism that predicts a decreasing step size with increasing load (17). However, additional factors may contribute to the observed short forward step size, including the potential influence of adaptor or microtubule-associated proteins (49–51) or posttranslational modifications (5), which were not present in the in vitro studies. In addition to the similarities

observed in the step distributions, discrepancies were noted in the incidence of backward steps when compared to previous in vitro studies (12, 14, 16). Our observations of the dynein tail revealed a lower incidence of backward steps ($p_{backward}$ = 0.04, Fig. 2H) in contrast to in vitro studies without load (~0.20) (12, 14, 16) and an even higher discrepancy when high load was applied (0.35 to 0.50) (16). This suggests that dynein is highly efficient in moving forward under endogenous conditions.

Naturally Occurring Direction Reversals Usually Follow a Rapid Mechanism Distinct from a Tug-of-War Model. It is widely accepted that multiple motors of opposite polarity are both anchored to the same intracellular cargo (2, 52, 53). Therefore, not only unidirectional but also bidirectional cargo movement has often been observed (21, 38, 40, 42). However, it is unclear how cargo directionality is controlled, whether by a stochastic process, typically referred to as a tug-of-war between motors of opposite polarity (54–56), regulated by adaptor or microtubule-associated proteins (49–51), posttranslational modifications of microtubules (5), or by separate transport of different parts of the motor complex (35). With MINFLUX, it is possible to observe not only a few steps of the cargo movement with high precision (21) but a single dynein itself over several hundred nanometers. This allowed us to distinguish between processive retrograde and anterograde movements and thus to observe direction reversals with single-step resolution.

To study direction reversals and pauses at a spatial and temporal scale that was previously hidden by the lack of spatiotemporal precision in live-cell observations (18, 35), we categorized all direction reversals and pauses between successive processive movements of both Halo-DHC and Halo-DIC traces (*SI Appendix*, Fig. S5 and *SI Appendix, Materials and Methods*). We observed a similarly high percentage of traces containing direction reversals (38.5% of traces), both anterograde to retrograde and retrograde to anterograde, as well as pauses (41.0% of traces) between processive anterograde or retrograde movements (Fig. 3A). As expected, this suggests that motors of

opposite polarity both act on the same cargo, possibly to bypass obstacles or as a means of regulation to reach the desired cargo destination (52, 53, 57). However, we also observed a large fraction of highly processive traces with neither reversals nor pauses (46.2% of traces), which could indicate the transport of different types of cargo in uninterrupted traces compared to traces with reversals and pauses.

Strikingly, direction reversals occurred on the order of the dwell times of single steps (Fig. 3B and *SI Appendix*, Table S5, compared to Fig. 2J), suggesting a rapid regulatory reversal mechanism (38, 42, 58, 59). This rapid reversal is obviously in contrast to a tug-of-war scheme (55, 56, 60). Even more strikingly, pauses lasted substantially longer than single steps and were ~10 times longer than the duration of direction reversals (Fig. 3B and *SI Appendix*, Table S5). Unexpectedly, we rarely observed discrete forward and backward steps within reversals or pauses (Fig. 3C; 10.2% of reversals or pauses), which may indicate dynein forward and backward stepping or clearly indicate a brief unregulated tug-of-war. Alternatively, this behavior could be the result of a slower regulatory mechanism that still allows for a brief mechanical competition of opposing motors (53). Altogether, we observed that rapid direction reversals are most common during axonal transport in living neurons, but in rare cases, motors (of opposite polarity) can still engage in a brief tug-of-war.

To obtain a comprehensive understanding of the pauses and reversals within the context of the overall movement, we constructed two Markov chains for the two potential reversal mechanisms. In calculating the transition probabilities between the states that constitute the Markov chains, both the occurrence and duration of processive movements, pauses, and reversals were considered and related to each other. One of the Markov chains depicts the case of a regulatory reversal mechanism, distinguishing between distinct pause and reversal states (*SI Appendix*, Fig. S6A). The second describes the unregulated stochastic mechanism (tug-of-war) and allows for processive movement to transition into a single pause state, from which movement can resume in either direction (*SI Appendix*, Fig. S6B). With regard
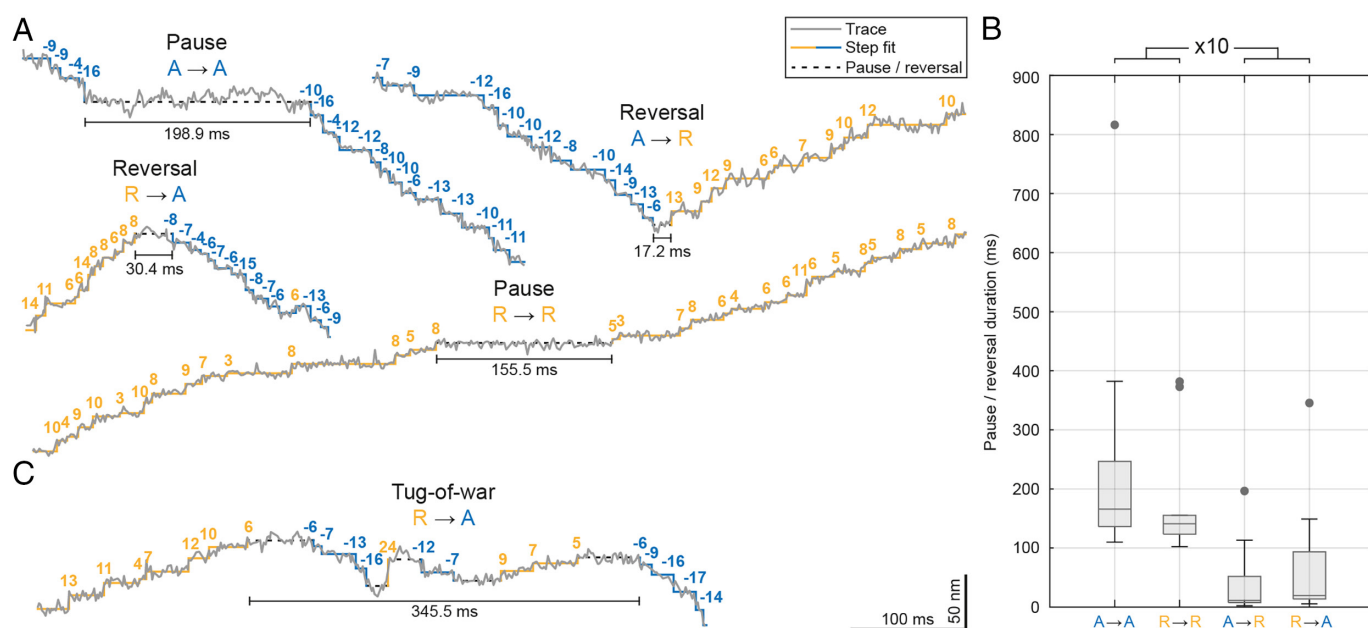

Fig. 3. Direction reversals occur rapidly at the time scale of single steps. (A) Extracts from example MINFLUX traces of dynein containing either a pause between anterograde (A → A) or retrograde (R → R) processive movement or a directional reversal from anterograde to retrograde (A → R) or retrograde to anterograde (R → A). (B) Boxplot showing that reversals (n = 24) have durations on the order of dwell times of single steps and last ten times shorter than pauses (n = 25). Gray dots indicate outliers. (C) Extract from an example MINFLUX trace showing a potential tug-of-war between retrograde and anterograde movement.

to the regulatory mechanism, the transition probabilities from processive movement into a pause or reversal are found to be similar for both directions ($p_{R,R\to R} \approx p_{R,R\to A}$, $p_{A,A\to A} \approx p_{A,A\to R}$). A comparison of the transition probabilities from pauses and reversals back to processive movement, however, reveals a striking disparity: Reversals are approximately four times less likely to persist than pauses, largely due to their markedly shorter duration, as discussed above (Fig. 3B). The stationary long-term probability for each state, π, indicates the processivity of endogenous dynein in both models, as π_R and π_A are larger than the probability of pause or reversal states. However, it should be acknowledged that the observed transition probabilities were derived from dynein being tracked in the mid-axon after six to nine days in culture and thus may differ when measured for other axonal regions and time points.

Compared to recent live-cell studies that also tracked dynein directly with conventional centroid localization (18, 35), the duration of reversals and pauses that we observed with MINFLUX was substantially shorter. This is because the lower spatiotemporal resolution of conventional tracking using single fluorophores or fluorescent proteins did not allow the detection of individual steps in living cells. Conversely, although we observed reversals and pauses of similar duration as previous widefield-based studies (Fig. 1 C and E), and although we obtained MINFLUX traces over the course of several seconds, we were unable to characterize long-lasting reversals or pauses on the order of seconds, most likely due to eventual photobleaching. Fig. 2F shows an example of a MINFLUX trace in which dynein transitioned to a nonprocessive state at the end of the trace (grayed out area), but the attached fluorophore likely underwent photobleaching before we could track a potential resumption after a pause or reversal on the order of seconds. Nonetheless, the single-step precision of MINFLUX clearly allows the characterization of naturally occurring direction reversals and pauses that were previously hidden, indicating a rapid regulatory reversal mechanism of bidirectional axonal transport in neurons.

Dynein Consumes one ATP to Perform a Step. Whether dynein consumes one or more ATPs per step has remained controversial since the first structural studies, because dynein's ring-shaped motor domain in principle allows ATP binding to four of its six ATPases associated with diverse cellular activities (AAA) domains (61). ATP hydrolysis at AAA1 has been shown to be essential for dynein motility (62). However, while it has been shown that AAA3 (63–65) and AAA4 (66) serve regulatory functions, it remains unknown whether ATP hydrolysis at AAA3 and/or AAA4 occur together with AAA1 to perform a single step, implying that dynein consumes two (or more) ATPs to perform a single step (20), remained the subject of debate.

To clarify whether dynein requires one or more ATPs to be hydrolyzed sequentially in order to perform a step, we performed a detailed analysis of the dwell times between consecutive steps of endogenous dynein. We compared three different models to describe the dwell time data, a single exponential decay and a convolution of two exponential decays with equal or unequal rate constants (Fig. 4 and *SI Appendix*, Fig. S7). To be independent of the data representation, we aimed to describe the data directly using maximum likelihood estimation. The model that best describes the data was determined using Akaike weights as a measure of the probability that one of the candidate models is the best, given the data and the three candidate models (67). According to this approach, the dwell time distribution was best described by a convolution of two exponentials with a low (k_1) and a high (k_2) rate constant (*SI Appendix*, Fig. S7 A and B). As our live-cell measurements were conducted at endogenous ATP concentrations and
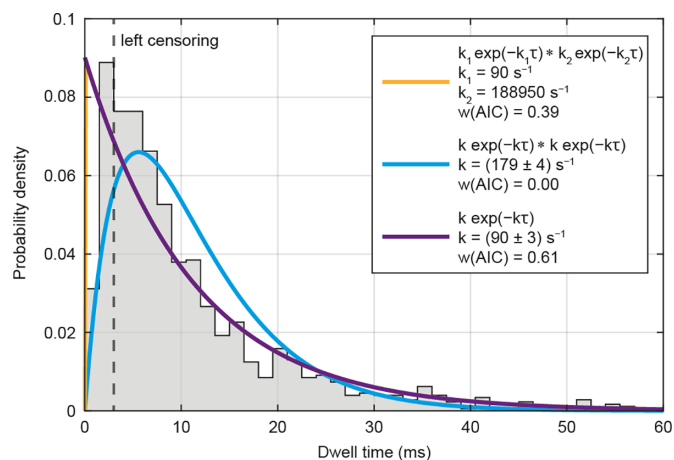

Fig. 4. Dynein consumes one ATP per step. Dwell time distribution of endogenous dynein (Halo-DHC and Halo-DIC) with three possible models for the description of the data (n = 1,178, N = 18). Left censoring of the distribution corresponds to the case where it is assumed that extremely fast steps ($\tau < 3$ ms) are partially missed and therefore underrepresented. Based on Akaike weights w(AIC), the single exponential model (purple) is the favored model for the description of the data in this case (i.e., one ATP per step). The orange curve, representing a convolution of two exponentials with unequal rate constants, overlaps exactly with the purple curve, and the low rate constant k_1 corresponds to that of the single exponential model, while the high rate constant k_2 becomes infinite. A convolution of two exponentials with the same rate constant (cyan) would correspond to a model in which dynein consumes two ATPs per step, but does not describe the data well. Totally, 212 data points were excluded by the left censoring.

thus are not necessarily rate-limited by ATP binding, the lower rate constant can be assigned to the rate-limiting step of the ATPase cycle, while the higher rate constant may be attributed to fast cycle steps. Actually, the high rate constant is in good agreement with the ATP hydrolysis and ADP dissociation rate of $\sim 1,000$ s^{-1} determined in biochemical assays (68), whereas the low rate constant matches the ATPase activity of purified dynein–dynactin–adaptor complexes (16). However, as the extremely fast steps ($\tau < 3$ ms) occur on a timescale close to the temporal resolution of our measurement, it is likely that they may be partially missed and thus underrepresented in the data. When considering only steps with dwell times $\tau < 3$ ms, the single exponential model with a rate constant of $k = (90 \pm 3)$ s^{-1} provides the best fit to the data (Fig. 4). Consequently, the low rate constant k_1 of the model with different rate constants becomes equal to the rate constant k of the single exponential model.

Both interpretations are consistent with different possible stepping mechanisms. One is an "alternating shuffle" (12), in which both head domains alternately take steps twice as large as the tail. The other is an "inchworm" model (15), in which one head domain takes the lead and the other head domain follows, which includes the possibility of uncoordinated head movement (13, 14). It is important to note that a convolution with two equal rate constants (i.e., two ATPs per step) does not adequately describe the data in either case. Instead, a single rate constant of ~ 90 s^{-1} describes the ATPase cycle of dynein at the observed timescale. While it cannot be definitely excluded that additional ATPs may be hydrolyzed independently, which are not necessary for the completion of a single step, our findings suggest that dynein consumes one ATP to perform a step, as proposed in in vitro studies (12, 16, 17, 48, 63), rather than two ATPs per step (20, 69).

In conclusion, MINFLUX localization enabled the direct tracking of CRISPR/Cas9-tagged endogenous dynein, revealing its stepping behavior in living primary neurons. The observation of mammalian dynein moving on the microtubule lattice revealed primarily 8 nm-sized steps, with frequent sideways but few

backward steps. Our high spatiotemporal precision enabled us to identify and characterize the fast changes in movement direction with a considerably enhanced level of detail, favoring a rapid regulated reversal mechanism over a stochastic tug-of-war. Finally, by analyzing the dwell times between steps, we conclude that dynein consumes one ATP to perform a step, which clarifies previous findings. Our study illustrates the importance of combining direct and specific labeling of the endogenous protein of interest with the nanometer/millisecond tracking precision of MINFLUX for an accurate description of protein dynamics in living cells.

Materials and Methods

A detailed description of the CRISPR/Cas9 knock-in construct design, sample preparation, MINFLUX and widefield data acquisition, and the data analysis can be found in *SI Appendix*.

Author affiliations: [a]Department of Optical Nanoscopy, Max Planck Institute for Medical Research, Heidelberg 69120, Germany; and [b]Department of NanoBiophotonics, Max Planck Institute for Multidisciplinary Sciences, Göttingen 37077, Germany

1. S. L. Reck-Peterson, W. B. Redwine, R. D. Vale, A. P. Carter, The cytoplasmic dynein transport machinery and its many cargoes. *Nat. Rev. Mol. Cell Biol.* **19**, 382–398 (2018).
2. S. Maday, A. E. Twelvetrees, A. J. Moughamian, E. L. Holzbaur, Axonal transport: Cargo-specific mechanisms of motility and regulation. *Neuron* **84**, 292–309 (2014).
3. J. N. Sleigh, A. M. Rossor, A. D. Fellows, A. P. Tosolini, G. Schiavo, Axonal transport and neurological disease. *Nat. Rev. Neurol.* **15**, 691–703 (2019).
4. M. Hafezparast *et al.*, Mutations in dynein link motor neuron degeneration to defects in retrograde transport. *Science* **300**, 808–812 (2003).
5. P. Guedes-Dias, E. L. F. Holzbaur, Axonal transport: Driving synaptic function. *Science* **366**, eaaw9997 (2019).
6. P. W. Baas, J. S. Deitch, M. M. Black, G. A. Banker, Polarity orientation of microtubules in hippocampal neurons: Uniformity in the axon and nonuniformity in the dendrite. *Proc. Natl. Acad. Sci. U.S.A.* **85**, 8335–8339 (1988).
7. B. M. Paschal, R. B. Vallee, Retrograde transport by the microtubule-associated protein MAP 1C. *Nature* **330**, 181–183 (1987).
8. L. Urnavicius *et al.*, Cryo-EM shows how dynactin recruits two dyneins for faster movement. *Nature* **554**, 202–206 (2018).
9. D. A. Grotjahn *et al.*, Cryo-electron tomography reveals that dynactin recruits a team of dyneins for processive motility. *Nat. Struct. Mol. Biol.* **25**, 203–207 (2018).
10. R. J. McKenney, W. Huynh, M. E. Tanenbaum, G. Bhabha, R. D. Vale, Activation of cytoplasmic dynein motility by dynactin-cargo adapter complexes. *Science* **345**, 337–341 (2014).
11. M. A. Schlager, H. T. Hoang, L. Urnavicius, S. L. Bullock, A. P. Carter, In vitro reconstitution of a highly processive recombinant human dynein complex. *EMBO J.* **33**, 1855–1868 (2014).
12. S. L. Reck-Peterson *et al.*, Single-molecule analysis of dynein processivity and stepping behavior. *Cell* **126**, 335–348 (2006).
13. W. Qiu *et al.*, Dynein achieves processive motion using both stochastic and coordinated stepping. *Nat. Struct. Mol. Biol.* **19**, 193–200 (2012).
14. M. A. DeWitt, A. Y. Chang, P. A. Combs, A. Yildiz, Cytoplasmic dynein moves through uncoordinated stepping of the AAA+ ring domains *Science* **335**, 221–225 (2012).
15. S. Niekamp, N. Stuurman, N. Zhang, R. D. Vale, Three-color single-molecule imaging reveals conformational dynamics of dynein undergoing motility. *Proc. Natl. Acad. Sci. U.S.A.* **118**, e2101391118. (2021).
16. M. M. Elshenawy *et al.*, Cargo adaptors regulate stepping and force generation of mammalian dynein-dynactin. *Nat. Chem. Biol.* **15**, 1093–1101 (2019).
17. R. Mallik, B. C. Carter, S. A. Lex, S. J. King, S. P. Gross, Cytoplasmic dynein functions as a gear in response to load. *Nature* **427**, 649–652 (2004).
18. N. A. Tirumala *et al.*, Single-molecule imaging of stochastic interactions that drive dynein activation and cargo movement in cells. *J. Cell Biol.* **223**, e202210026 (2024).
19. A. E. Twelvetrees *et al.*, The dynamic localization of cytoplasmic dynein in neurons is driven by kinesin-1. *Neuron* **90**, 1000–1015 (2016).
20. C. S. Peng *et al.*, Nanometer-resolution tracking of single cargo reveals dynein motor mechanisms. *Nat. Chem. Biol.* (2024), 10.1038/s41589-024-01694-2.
21. C. Kural *et al.*, Kinesin and dynein move a peroxisome in vivo: A tug-of-war or coordinated movement?. *Science* **308**, 1469–1472 (2005).
22. X. Nan, P. A. Sims, P. Chen, X. S. Xie, Observation of individual microtubule motor steps in living cells with endocytosed quantum dots. *J. Phys. Chem. B* **109**, 24220–24224 (2005).
23. J. O. Wirth *et al.*, MINFLUX dissects the unimpeded walking of kinesin-1. *Science* **379**, 1004–1010 (2023).
24. T. Deguchi *et al.*, Direct observation of motor protein stepping in living cells using MINFLUX. *Science* **379**, 1010–1015 (2023).
25. F. Balzarotti *et al.*, Nanometer resolution imaging and tracking of fluorescent molecules with minimal photon fluxes. *Science* **355**, 606–612 (2017).
26. Y. Eilers, H. Ta, K. C. Gwosch, F. Balzarotti, S. W. Hell, MINFLUX monitors rapid molecular jumps with superior spatiotemporal resolution. *Proc. Natl. Acad. Sci. U.S.A.* **115**, 6117–6122 (2018).
27. S. J. King, C. L. Brown, K. C. Maier, N. J. Quintyne, T. A. Schroer, Analysis of the dynein-dynactin interaction in vitro and in vivo. *Mol. Biol. Cell* **14**, 5089–5097 (2003).
28. P. S. Vaughan, J. D. Leszyk, K. T. Vaughan, Cytoplasmic dynein intermediate chain phosphorylation regulates binding to dynactin. *J. Biol. Chem.* **276**, 26171–26179 (2001).
29. M. Ratz, I. Testa, S. W. Hell, S. Jakobs, CRISPR/Cas9-mediated endogenous protein tagging for RESOLFT super-resolution microscopy of living human cells. *Sci. Rep.* **5**, 9592 (2015).
30. J. Willems *et al.*, ORANGE: A CRISPR/Cas9-based genome editing toolbox for epitope tagging of endogenous proteins in neurons. *PLoS Biol.* **18**, e3000665 (2020).
31. G. V. Los *et al.*, HaloTag: A novel protein labeling technology for cell imaging and protein analysis. *ACS Chem. Biol.* **3**, 373–382 (2008).
32. L. Wang *et al.*, A general strategy to develop cell permeable and fluorogenic probes for multicolour nanoscopy. *Nat. Chem.* **12**, 165–172 (2020).
33. P. Mangeol, B. Prevo, E. J. Peterman, KymographClear and KymographDirect: Two tools for the automated quantitative analysis of molecular and cellular dynamics using kymographs. *Mol. Biol. Cell* **27**, 1948–1957 (2016).
34. S. M. Shih *et al.*, Intraflagellar transport drives flagellar surface motility. *Elife* **2**, e00744 (2013).
35. A. D. Fellows, M. Bruntraeger, T. Burgold, A. R. Bassett, A. P. Carter, Dynein and dynactin move long-range but are delivered separately to the axon tip. *J. Cell Biol.* **223**, e202309084 (2024).
36. R. L. Morris, P. J. Hollenbeck, The regulation of bidirectional mitochondrial transport is coordinated with axonal outgrowth. *J Cell Sci* **104**, 917–927 (1993).
37. V. Soppina, A. K. Rai, A. J. Ramaiya, P. Barak, R. Mallik, Tug-of-war between dissimilar teams of microtubule motors regulates transport and fission of endosomes. *Proc. Natl. Acad. Sci. U.S.A.* **106**, 19381–19386 (2009).
38. S. E. Encalada, L. Szpankowski, C. H. Xia, L. S. Goldstein, Stable kinesin and dynein assemblies drive the axonal transport of mammalian prion protein vesicles. *Cell* **144**, 551–565 (2011).
39. M. van Spronsen *et al.*, TRAK/Milton motor-adaptor proteins steer mitochondrial trafficking to axons and dendrites. *Neuron* **77**, 485–502 (2013).
40. S. Maday, K. E. Wallace, E. L. Holzbaur, Autophagosomes initiate distally and mature during transport toward the cell soma in primary neurons. *J. Cell Biol.* **196**, 407–417 (2012).
41. T. Kobayashi, T. Murayama, Cell cycle-dependent microtubule-based dynamic transport of cytoplasmic dynein in mammalian cells. *PLoS One* **4**, e7827 (2009).
42. M. M. Fu, E. L. Holzbaur, JIP1 regulates the directionality of APP axonal transport by coordinating kinesin and dynein motors. *J. Cell Biol.* **202**, 495–508 (2013).
43. J. B. Grimm *et al.*, A general method to improve fluorophores using deuterated auxochromes. *JACS Au* **1**, 690–696 (2021).
44. R. Schmidt *et al.*, MINFLUX nanometer-scale 3D imaging and microsecond-range tracking on a common fluorescence microscope. *Nat. Commun.* **12**, 1478 (2021).
45. L. Loeff, J. W. J. Kerssemakers, C. Joo, C. Dekker, AutoStepfinder: A fast and automated step detection method for single-molecule analysis. *Patterns* **2**, 100256 (2021).
46. L. S. Ferro, S. Can, M. A. Turner, M. M. ElShenawy, A. Yildiz, Kinesin and dynein use distinct mechanisms to bypass obstacles. *Elife* **8**, e48629 (2019).
47. S. Chaaban, A. P. Carter, Structure of dynein-dynactin on microtubules shows tandem adaptor binding. *Nature* **610**, 212–216 (2022).
48. S. Toba, T. M. Watanabe, L. Yamaguchi-Okimoto, Y. Y. Toyoshima, H. Higuchi, Overlapping hand-over-hand mechanism of single molecular motility of cytoplasmic dynein. *Proc. Natl. Acad. Sci. U.S.A.* **103**, 5741–5745 (2006).
49. J. T. Canty, A. Hensley, M. Aslan, A. Jack, A. Yildiz, TRAK adaptors regulate the recruitment and activation of dynein and kinesin in mitochondrial transport. *Nat. Commun.* **14**, 1376 (2023).
50. L. S. Ferro *et al.*, Structural and functional insight into regulation of kinesin-1 by microtubule-associated protein MAP7. *Science* **375**, 326–331 (2022).
51. R. Dixit, J. L. Ross, Y. E. Goldman, E. L. Holzbaur, Differential regulation of dynein and kinesin motor proteins by tau. *Science* **319**, 1086–1089 (2008).
52. M. A. Welte, Bidirectional transport along microtubules. *Curr. Biol.* **14**, R525–R537 (2004).
53. W. O. Hancock, Bidirectional cargo transport: Moving beyond tug of war. *Nat. Rev. Mol. Cell Biol.* **15**, 615–628 (2014).
54. R. D. Vale, F. Malik, D. Brown, Directional instability of microtubule transport in the presence of kinesin and dynein, two opposite polarity motor proteins. *J. Cell Biol.* **119**, 1589–1596 (1992).
55. A. G. Hendricks *et al.*, Motor coordination via a tug-of-war mechanism drives bidirectional vesicle transport. *Curr. Biol.* **20**, 697–702 (2010).
56. M. J. Muller, S. Klumpp, R. Lipowsky, Tug-of-war as a cooperative mechanism for bidirectional cargo transport by molecular motors. *Proc. Natl. Acad. Sci. U.S.A.* **105**, 4609–4614 (2008).
57. A. Yildiz, Y. Zhao, Dyneins. *Curr. Biol.* **33**, R1274–R1279 (2023).
58. S. Heber *et al.*, Tropomyosin 1-I/C coordinates kinesin-1 and dynein motors during oskar mRNA transport. *Nat. Struct. Mol. Biol.* **31**, 476–488 (2024), 10.1038/s41594-024-01212-x.
59. A. Kunwar *et al.*, Mechanical stochastic tug-of-war models cannot explain bidirectional lipid-droplet transport. *Proc. Natl. Acad. Sci. U.S.A.* **108**, 18960–18965 (2011).
60. A. I. D'Souza, R. Grover, G. A. Monzon, L. Santen, S. Diez, Vesicles driven by dynein and kinesin exhibit directional reversals without regulators. *Nat. Commun.* **14**, 7532 (2023).
61. T. Kon *et al.*, The 2.8 Å crystal structure of the dynein motor domain. *Nature* **484**, 345–350 (2012).

62. T. Kon, M. Nishiura, R. Ohkura, Y. Y. Toyoshima, K. Sutoh, Distinct functions of nucleotide-binding/hydrolysis sites in the four AAA modules of cytoplasmic dynein. *Biochemistry* **43**, 11266–11274 (2004).

63. M. A. DeWitt, C. A. Cypranowska, F. B. Cleary, V. Belyy, A. Yildiz, The AAA3 domain of cytoplasmic dynein acts as a switch to facilitate microtubule release. *Nat. Struct. Mol. Biol.* **22**, 73–80 (2015).

64. G. Bhabha *et al.*, Allosteric communication in the dynein motor domain. *Cell* **159**, 857–868 (2014).

65. M. P. Nicholas *et al.*, Cytoplasmic dynein regulates its attachment to microtubules via nucleotide state-switched mechanosensing at multiple AAA domains. *Proc. Natl. Acad. Sci. U.S.A.* **112**, 6371–6376 (2015).

66. X. Liu, L. Rao, A. Gennerich, The regulatory function of the AAA4 ATPase domain of cytoplasmic dynein. *Nat. Commun.* **11**, 5952 (2020).

67. K. P. Burnham, D. R. Anderson, *Model Selection and Multimodel Inference: A Practical Information-Theoretic Approach* (Springer, New York, 2002).

68. E. L. Holzbaur, K. A. Johnson, Microtubules accelerate ADP release by dynein. *Biochemistry* **28**, 7010–7016 (1989).

69. J. L. Ross, K. Wallace, H. Shuman, Y. E. Goldman, E. L. Holzbaur, Processive bidirectional motion of dynein-dynactin complexes in vitro. *Nat. Cell Biol.* **8**, 562–570 (2006).